CrossMark

Enhanced proton acceleration from laser interaction with curved surface nanowire targets

Xueming Li [1],†, **Yue Chao**[2], **Deji Liu**[1], **Shutong Zhang**[2], **Zhanjun Liu**[1,2], **Lihua Cao**[1,2],† **and Chunyang Zheng**[1,2]

[1]Institute of Applied Physics and Computational Mathematics, Beijing, 100094, PR China

[2]Center for Applied Physics and Technology, HEDPS, School of Physics and College of Engineering, Peking University, Beijing 100871, PR China

A novel curved surface nanowire target is proposed to improve the cutoff energy of accelerated protons via target normal sheath acceleration. The interaction of a laser of intensity 1.37×10^{20} W cm^{-2} with a curved surface nanowire target is studied by two-dimensional particle-in-cell simulations. The numerical results indicate that the sheath electric field at the target rear side is significantly enhanced by this simple target design, compared with using the planar nanowire target. The transverse motion of hot electrons is effectively confined and the energy density of electrons is naturally increased. A series of simulations with various target parameters is carried out to investigate the performance of this novel target. This tailored target may provide implications for generating high-quality proton beams in experiments.

Key words: plasma applications, plasma simulation, intense particle beams

1. Introduction

The interaction of ultra-intense short laser pulses with plasma has been proposed as a significant mechanism for high-energy particles in the last decades. In particular, energetic ion beams have a multitude of promising potential applications in many areas, such as proton radiography (Borghesi *et al.* 2004), tumour therapy (Fourkal *et al.* 2002), materials characterization (Passoni, Fedeli & Mirani 2019; Mirani *et al.* 2021; Boivin *et al.* 2022) and fast ignition in inertial confinement fusion (Tabak *et al.* 1994), etc. Several mechanisms for laser-driven ion acceleration have been developed, including target normal sheath acceleration (TNSA) (Snavely *et al.* 2000; Wilks *et al.* 2001; Mora 2003), radiation pressure acceleration (Robinson *et al.* 2008; Yan *et al.* 2008), collisionless shock acceleration (Xie *et al.* 2019; Tochitsky *et al.* 2020), magnetic vortex acceleration (Bulanov *et al.* 2010; Nakamura *et al.* 2010; Li *et al.* 2022), etc. Among these, TNSA has been studied widely both in simulations and experiments (Maksimchuk *et al.* 2000; Wagner *et al.* 2016; Lv *et al.* 2019). In this scheme, the incident laser pulse irradiates the solid target and the electrons at the front surface are heated and accelerated. The hot electrons propagating forward can penetrate through the target, creating a charge-separation electric field in the vacuum space near the rear of the target. The electric field, several teravolts per

† Email addresses for correspondence: lixueming20@gscaep.ac.cn, cao_lihua@iapcm.ac.cn

metre, is strong enough to ionize the hydrogen atoms and accelerate the resulting protons, which are usually from water or hydrocarbon contaminants attached to the target surface (Chao *et al.* 2022).

In TNSA, the quality of accelerated protons is determined by hot electrons from the target, which depend on the intensity of the incident laser and the absorption of laser energy by the plasma. Compared with increasing the laser intensity, improving the laser-to-electron energy conversion efficiency is more likely for implementation for the sake of high-quality protons. An effective way to enhance the energy coupling efficiency from the laser to the electrons is using targets with a structured front surface. There has been a good deal of effort put into investigating the effect of structured targets on laser–plasma coupling, including double-layer targets (Yang *et al.* 2018), cone targets (Honrubia, Morace & Murakami 2017), nanotube targets (Chatterjee *et al.* 2012) and nano-structured targets (Zhao *et al.* 2010; Xie *et al.* 2020; Blanco *et al.* 2017), etc. Thus, a high-contrast laser is required to prevent the surface structures from being damaged or destroyed before the main laser pulse arrives (Calestani *et al.* 2021).

For a flat solid foil target irradiated by the incident laser, the laser pulse is largely reflected at the plasma critical density. By contrast, a nanowire target which has a stack of thin plasma layers at subwavelength spacing grown on a thin metallic substrate (Cao *et al.* 2010; Wang *et al.* 2012; Yu *et al.* 2012) is beneficial to generate more hot electrons. The complex geometry enables the laser pulse to interact for an extended distance with the inner volume of the target. As mentioned in previous studies (Feng *et al.* 2018), electrons within the nanowires will be pulled out by the laser field and accelerated by direct laser acceleration. Ultimately, these electrons, gaining considerable kinetic energy, will set up an enhanced sheath field for TNSA. For a laser pulse with Gaussian profile in the transverse direction, the sheath field in the target rear surface also appears as a Gaussian shape. The most energetic protons come from the axial position of the sheath field, so it is of prime importance to suppress the transverse diffusion of hot electrons. To achieve this goal, a strong magnetic field of more than $10\,000$ T has been applied in the longitudinal direction in some previous simulation works (Gong *et al.* 2017; Kuri, Das & Patel 2017), but it is still very challenging and not practical to reach such strength in experiments for now.

In this study, we proposed a novel tailored target referred to as a curved surface nanowire target (CSNT), which originates from a planar nanowire target (PNT) but surfaces of both the nanowires and the substrate are curved. For convenience, a schematic diagram is plotted in figure 1(*c*) to illustrate the features of two kinds of targets. The yellow part is the nanowire target, the grey part is the hydrogen layer and the light blue part donates the electron cloud. A large proportion of hot electrons at $\lambda_0/2$ (λ_0 is the laser wavelength) intervals are pulled out from the nanowires by the periodic laser electric field and accelerated forward, and then, they transport to the rear surface of the target. An electron cloud is formed and a strong charge-separation field is also established there to accelerate the protons from the hydrogen layer. The design of the CSNT aims to reduce the reflection and enhance the absorption of the incident laser, and meanwhile plays a better role in constraining the transverse motion of hot electrons. Given the technological advances in the fabrication of nano-structured targets, a possible way to realize such a kind of target is 3D printing using the two-photon polymerization (2PP) additive manufacturing technique (Bailly-Grandvaux *et al.* 2020). Here, a series of two-dimensional (2-D) particle-in-cell (PIC) simulations are carried out to compare the CSNT and the PNT.

This work is organized as follows. In § 2, the simulation set-up and target parameters are presented. In § 3, the enhancement of TNSA using the CSNT is shown in simulation
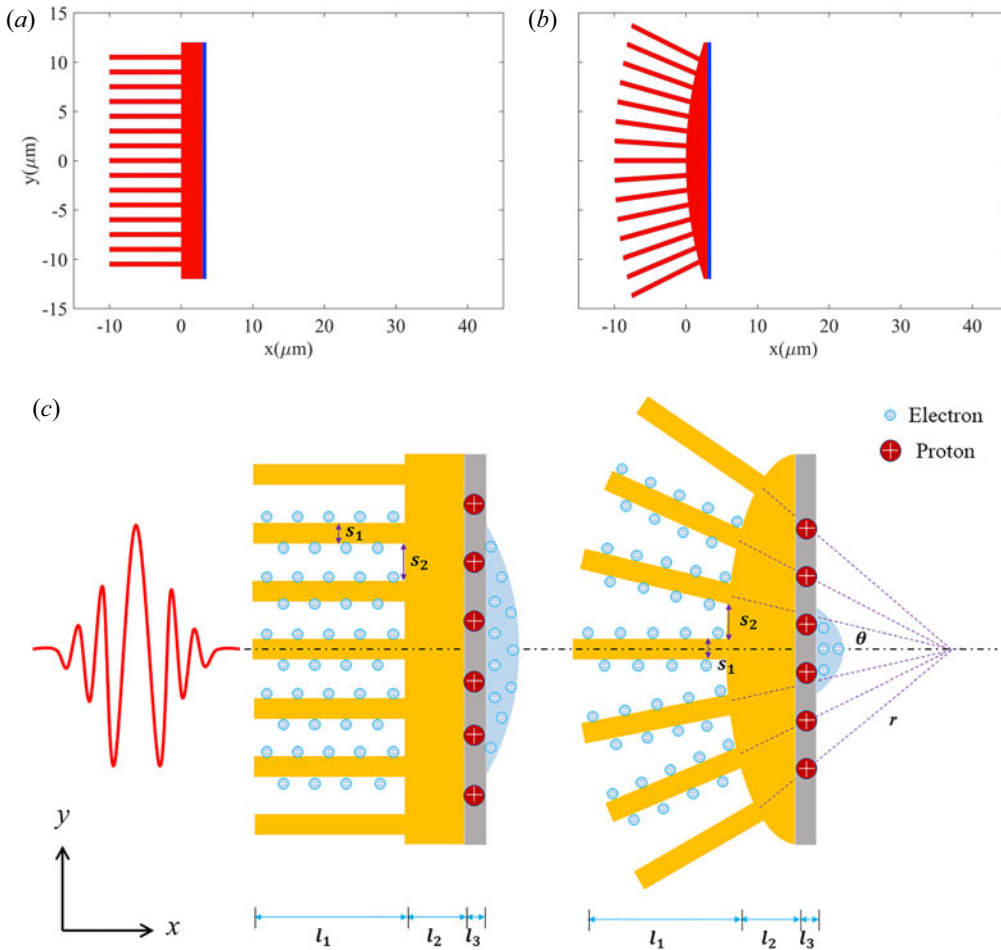
FIGURE 1. Target configurations of the PNT (*a*) and the CSNT (*b*) in the simulations. Both targets consist of nanowires and substrate of Au^{10+} (red), and a thin hydrogen foil (blue) adheres to the target rear. (*c*) Schematics of the planar nanowire target (*a*) and the curved surface nanowire target (*b*).

results in detail. In addition, the robustness of the CSNT is examined by a simulation scan over the target parameters. The conclusions are summarized in § 4.

2. Simulation set-up

Our 2-D simulations use relativistic PIC code EPOCH (Arber *et al.* 2015). The simulation box is $x \times y = 60\ \mu m \times 30\ \mu m$, which is divided into 4000×3000 cells, and each cell is filled with 100 electrons, 10 gold ions and 100 hydrogen ions. The grid mesh spacing is enough to resolve the minimum characteristic scale of the problem. The time resolution is decided by the spatial resolution, according to the Courant-Friedrichs-Lewy (CFL) condition. The left boundary conditions of the fields are so-called simple laser, which allow electromagnetic (EM) waves to propagate with as little reflection as possible and particles are fully transmitted so this is a reasonable choice for the boundary at which the EM pulse enters the simulation box. The top, bottom and right conditions of fields and the boundaries of the particles are all open. A p-polarized laser pulse with a wavelength

of $\lambda_0 = 0.8\ \mu$m and waist $w = 8\ \mu$m is incident from the left boundary of the simulation domain. The laser pulse has a Gaussian spatial profile, and a flat-top temporal shape with a duration of $16\,T_0$, including a rising edge of $2\,T_0$ and a descending edge of $2\,T_0$, where T_0 is the laser period. The peak intensity is $I_0 \sim 1.37 \times 10^{20}$ W cm^{-2}, corresponding to the normalized vector potential $a_0 = 8$.

The regular PNT consists of three parts, which appear as a comb structure, shown in figure 1(a). The first part is nanowires made of Au with diameters $s_1 = 0.5\ \mu$m, vacuum spacing $s_2 = 1\ \mu$m and length $l_1 = 10\ \mu$m. They are assumed to be pre-ionized Au^{10+} with density of $n_i = 5n_c$ and a corresponding electron density of $n_e = 50\,n_c$, where $n_c = m_e \omega_0^2 \epsilon_0/e^2$ is the critical density, m_e is the electron mass, ϵ_0 is the vacuum permittivity and e is the unit charge. The second part is a substrate of the same materials with a thickness of $l_2 = 3\ \mu$m. The nanowires and the substrate are placed in the region $-10\ \mu$m $< x < 3\mu$m and $-12\ \mu$m $< y < 12\ \mu$m. The third part is a 0.5 μm thick ($l_3 = 0.5\ \mu$m) and 12 μm wide hydrogen plasma layer attached to the rear of the substrate, with $n_H = n_e = 10\,n_c$, in the region $3\ \mu$m $< x < 3.5\ \mu$m and $-12\ \mu$m $< y < 12\ \mu$m.

The CSNT resembles the PNT, except that the front surface of the substrate is curved and the nanowire arrays extend in a radial pattern. That is, the profiles of the surface of the nanowire and the substrate appear to be in concentric circles. The vacuum spacing of nanowires in CSNT is approximately $s_2 = 1\ \mu$m, as seen in figure 1(b). Moreover, the diameter of the nanowire, the length, density and location are the same as the PNT. In our simulations, the parameter scope of the radius of curvature of the substrate r is from 30 μm to 500 μm. The centre of the circle of curvature is located on the x-axis and the horizontal distance from the y-axis is equal to the radius of curvature r. In order to ensure comparability with the PNT, the minimum value of r is set as 30 μm so that the thickness of the substrate and the number of nanowires in two cases can be nearly equivalent. Here, the central angle, as a more intuitive variable, is governed by the vacuum spacing of nanowires in the CSNT and the radius of curvature of the substrate: $\theta = (s_1 + s_2)/r$. The almost same central angle is set between each of two nanowires.

3. Simulation results and discussion

3.1. *Laser absorption and hot electron generation*

In the typical TNSA regime, a flat solid target is irradiated by an intense laser pulse to generate hot electrons which are heated by vacuum heating and the $J \times B$ acceleration. Hot electrons set up a sheath electric field at the surface of the target for proton acceleration. However, the laser pulse can only travel several skin depths into the target, so that a great amount of energy is reflected. Figure 2 shows the longitudinal Poynting flux S_x normalized by $(m_e\omega_0 c/e)^2$ at $t = 20\,T_0$. Both incident and reflected components of the Poynting flux can be observed at this moment. Compared with the PNT, the reflected component is weaker in the CSNT. The reflectivity can be estimated by integrating the Poynting flux S_- propagating in the negative direction at the left boundary, expressed as

$$R = \frac{\displaystyle\int_{y_{\min}}^{y_{\max}} \int_0^t S_-(x = 0)}{w_0},\tag{3.1}$$

where w_0 is the total energy of the incident laser pulse. The value of R determines the energy that flows into the target, which is closely linked to the temperature of the hot electrons. The reflectivity in the PNT is 22 %, while in the CSNT it is only 17 %. This result indicates that, in the CSNT, more energy is transferred to the electrons within the nanowires.
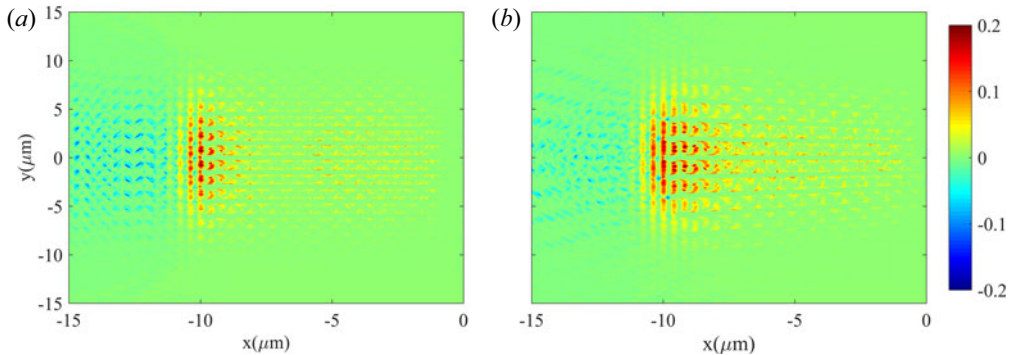
FIGURE 2. The longitudinal Poynting flux S_x normalized by $(m_e\omega_0 c/e)^2$ at $t = 20\,T_0$ for the PNT (a) and the CSNT (b).

The energy density distributions of hot electrons in two cases at $t = 30\,T_0$ are presented in figures 3(a) and 3(b), which are normalized by $n_c m_e c^2$. It is clear that the energy density of hot electrons in the CSNT is apparently higher than that in the PNT. A large number of high energy density electrons are pulled out from the nanowires by the periodic laser electric field and accelerated forward, and eventually they are transported to the centre region of the target rear surface. The convergence caused by the geometry of the CSNT counteracts part of the lateral diffusion, and thus the distribution of hot electrons is more concentrated at the rear of the target in the CSNT. To further certify the convergence effect of the CSNT, the profiles of energy density along the x-axis are plotted in figure 3(c) to reveal the comparison of the two cases, which profiles are averaged over the target rear surface region. The transverse motion of hot electrons is effectively confined and the energy density of the electrons is naturally increased in the CSNT. Furthermore, the energy spectra of electrons in both cases are exhibited in figure 3(d). It can be seen that, due to more effective heating, the number of electrons with high energy in the CSNT is higher than that in the PNT. Counting all electrons moving forward, the maximum energy of hot electrons in the CSNT is over 47 MeV, compared with a maximum energy of only 30 MeV in the PNT. The temperature of the hot electrons T_h has increased from 3.8 to 5.3 MeV, which can be obtained by fitting the spectra with a Maxwellian distribution, as given by the dashed line in 3(d). As discussed above, due to the higher energy conversion efficiency from the laser to electrons, the temperature of the electrons in the CSNT increases as expected.

3.2. *Sheath filed and proton acceleration*

As hot electrons originating from the nanowires propagate through the target rear, a longitudinal sheath field is established, and it can be estimated as (Arefiev, Toncian & Fiksel 2016)

$$E_{\text{sheath}} \sim \sqrt{n_e T_e}, \qquad (3.2)$$

where n_e, T_e are the density of hot electrons and characteristic kinetic energy, respectively. The characteristic scale of the sheath is the Debye length $\lambda_D = \sqrt{\epsilon_0 T_e / n_e e^2}$. According to (3.2), the sheath field is proportional to the square root of the product of the number density and temperature of hot electrons. The strong sheath field is determined by the ability of the laser pulse to generate copious energetic electrons. Figure 4 shows the sheath field near the rear of the target of two cases at $t = 30 T_0$. The moment is chosen when the longitudinal electric field reaches its peak value in our simulations. As performed in
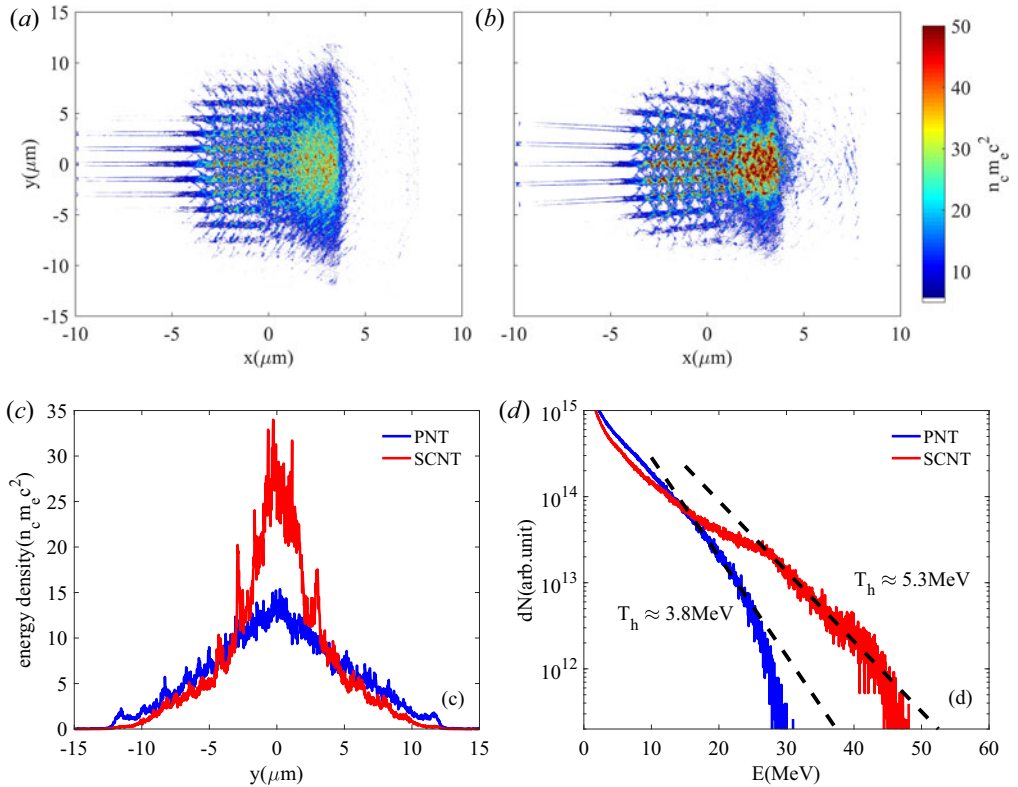
FIGURE 3. Energy density of hot electrons in the PNT (*a*) and in the CSNT (*b*) at $t = 30\,T_0$. (*c*) Averaged energy density of hot electrons along the *y* direction within the region $-15\,\mu\text{m} < x < 3\,\mu\text{m}$. (*d*) The energy spectra of hot electrons at $t = 30\,T_0$.

figures 4(*a*) and 4(*b*), it is found that the longitudinal electric field in the CSNT is more localized in the transverse direction, which is closer to the axis $y = 0$. On the other hand, the electric field in the CSNT occupies a larger area compared with that in the PNT, that is, the characteristic scale of the sheath electric field in the CSNT is larger than that in the PNT. From figure 4(*c*), one can see that the amplitude of electric field along the *x*-axis at $y = 0$ in the CSNT exceeds that in the PNT. It is obvious that the amplification of the sheath electric field in the CSNT is more than 20 % compared with the PNT.

As shown in figure 5, the energy spectra of protons at the end of the simulation exhibit a similar Boltzmann distribution, which is a typical spectral shape of TNSA. The proton cutoff energy in the CSNT is evidently higher than that in the PNT, which is in accordance with the snapshots of the sheath field of two kinds of target. Using this tailored target design, the cutoff energy increase from 50 to 73 MeV. We count these energetic protons and find that the energy conversion efficiency from laser to forward protons with energy above 5 MeV is 11.6 % in the PNT and 14.2 % in the CSNT. The simulation results demonstrated that the CSNT has better performance than the PNT in generating high-energy protons.

To study the robustness of the CSNT, several central angles, corresponding to different radii of curvature of the curved surface nanowire target, are adopted in different simulation cases. The radii of curvature of the curved surface nanowire target vary from 30 to 500μm, and the corresponding central angle $\theta = 0.05, 0.037, 0.03, 0.021, 0.015, 0.01$ and 0.003

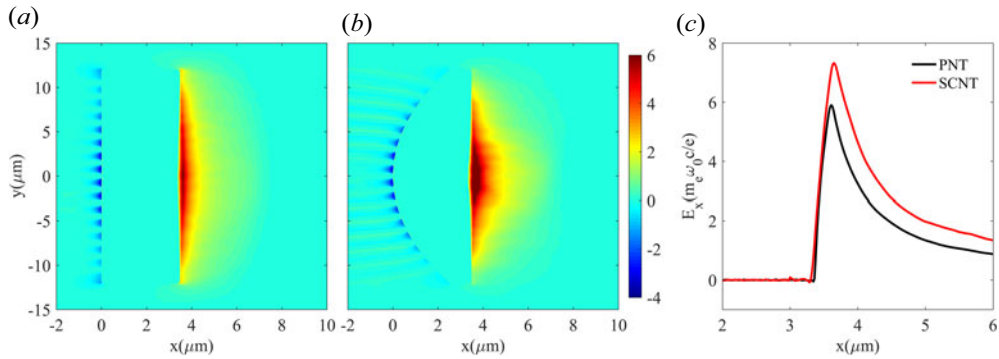FIGURE 4. Longitudinal electric fields E_x at $t = 30T_0$ near the target rear surface for (*a*) the PNT and (*b*) the CSNT. (*c*) The corresponding slices of E_x along the *x*-axis, averaged near the region $y = 0$. Here, E_x is normalized by $m_e\omega_0 c/e$.
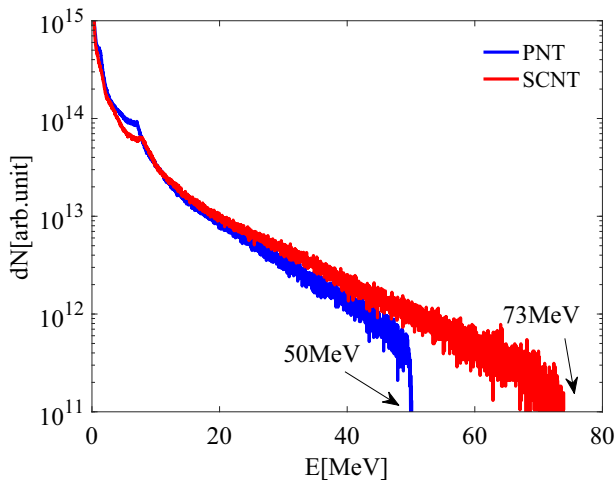

FIGURE 5. The proton energy spectra in the PNT (blue) and in the CSNT (red) at the end of simulation.

radians. As the radius of curvature of the curved surface nanowire increases, the central angle of the nanowires decreases. Finally, the matching relation of the central angle and the radius of curvature can be extrapolated to the limiting case $\theta = 0$, namely, the case of the planar nanowire target. The cutoff energy of protons and the conversion efficiency with different central angles are shown in figures 6(*a*) and 6(*b*). For the CSNT with different radii of curvature of nanowires, both the cutoff energy and the conversion efficiency nearly linearly increase with the central angle. Besides, the cutoff energy of protons and the conversion efficiency in the CSNT are higher than those in the PNT. It is clear that this target design can significantly increase the cutoff energy and the number of accelerated protons.

4. Conclusions

In summary, 2-D PIC simulations are performed to study the improvement of a novel nanowire target on laser-driven proton acceleration in TNSA. By using a curved nanowire target, the electron energy density is significantly improved compared with that in a planar
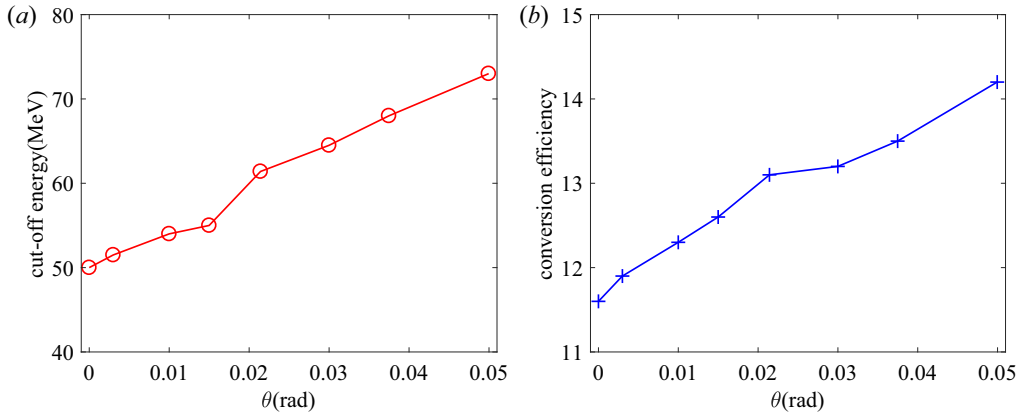
FIGURE 6. The dependence of (*a*) cutoff energy and (*b*) conversion efficiency of protons on different central angles.

nanowire target, and thereby the sheath electric field is enhanced. A series of simulations with varied central angles of the nanowires is employed to reveal the effectiveness of CSNT. With the increase in the central angle, the cutoff energy of protons and conversion efficiency clearly increase. Our simulation results show that the cutoff energy and the number of accelerated protons in the CSNT are superior to those in the PNT. This enhancement can be attributed to suppressed transverse diffusion of hot electrons and enhanced absorption of laser energy. This scheme could be helpful in generating high-quality proton beams in experiments without requiring higher laser intensity.

Acknowledgements

Editor Victor Malka thanks the referees for their advice in evaluating this article.

Declaration of interests

The authors report no conflict of interest.

REFERENCES

ARBER, T.D., BENNETT, K., BRADY, C.S., LAWRENCE-DOUGLAS, A., RAMSAY, M.G., SIRCOMBE, N.J., GILLIES, P., EVANS, R.G., SCHMITZ, H., BELL, A.R., *et al.* 2015 Contemporary particle-in-cell approach to laser-plasma modelling. *Plasma Phys. Control. Fusion* **57** (11), 113001.

AREFIEV, A., TONCIAN, T. & FIKSEL, G. 2016 Enhanced proton acceleration in an applied longitudinal magnetic field. *New J. Phys.* **18** (10), 105011.

BAILLY-GRANDVAUX, M., KAWAHITO, D., MCGUFFEY, C., STREHLOW, J., EDGHILL, B., WEI, M.S., ALEXANDER, N., HAID, A., BRABETZ, C., BAGNOUD, V., *et al.* 2020 Ion acceleration from microstructured targets irradiated by high-intensity picosecond laser pulses. *Phys. Rev.* E **102**, 021201.

BLANCO, M., FLORES-ARIAS, M.T., RUIZ, C. & VRANIC, M. 2017 Table-top laser-based proton acceleration in nanostructured targets. *New J. Phys.* **19** (3), 033004.

BOIVIN, F., VALLIÈRES, S., FOURMAUX, S., PAYEUR, S. & ANTICI, P. 2022 Quantitative laser-based x-ray fluorescence and particle-induced x-ray emission. *New J. Phys.* **24** (5), 053018.

BORGHESI, M., MACKINNON, A.J., CAMPBELL, D.H., HICKS, D.G., KAR, S., PATEL, P.K., PRICE, D., ROMAGNANI, L., SCHIAVI, A. & WILLI, O. 2004 Multi-MeV proton source investigations in ultraintense laser-foil interactions. *Phys. Rev. Lett.* **92**, 055003.

BULANOV, S.S., BYCHENKOV, V.Y., CHVYKOV, V., KALINCHENKO, G., LITZENBERG, D.W., MATSUOKA, T., THOMAS, A.G.R., WILLINGALE, L., YANOVSKY, V., KRUSHELNICK, K., *et al.* 2010 Generation of GeV protons from 1 PW laser interaction with near critical density targets. *Phys. Plasmas* **17** (4), 043105.

CALESTANI, D., VILLANI, M., CRISTOFORETTI, G., BRANDI, F., KOESTER, P., LABATE, L. & GIZZI, L.A. 2021 Fabrication of ZnO-nanowire-coated thin-foil targets for ultra-high intensity laser interaction experiments. *Matter Radiat. Extrem.* **6** (4), 046903.

CAO, L., GU, Y., ZHAO, Z., CAO, L., HUANG, W., ZHOU, W., HE, X.T., YU, W. & YU, M.Y. 2010 Enhanced absorption of intense short-pulse laser light by subwavelength nanolayered target. *Phys. Plasmas* **17** (4), 043103.

CHAO, Y., CAO, L., ZHENG, C., LIU, Z. & HE, X. 2022 Enhanced proton acceleration from laser interaction with a tailored nanowire target. *Appl. Sci.* **12** (3), 1153.

CHATTERJEE, G., SINGH, P.K., AHMED, S., ROBINSON, A.P.L., LAD, A.D., MONDAL, S., NARAYANAN, V., SRIVASTAVA, I., KORATKAR, N., PASLEY, J., *et al.* 2012 Macroscopic transport of mega-ampere electron currents in aligned carbon-nanotube arrays. *Phys. Rev. Lett.* **108**, 235005.

FENG, B., JI, L.L., SHEN, B.F., GENG, X.S., GUO, Z., YU, Q., XU, T.J. & ZHANG, L.G. 2018 Effects of micro-structures on laser-proton acceleration. *Phys. Plasmas* **25** (10), 103109.

FOURKAL, E., SHAHINE, B., DING, M., LI, J.S., TAJIMA, T. & MA, C.-M. 2002 Particle in cell simulation of laser-accelerated proton beams for radiation therapy. *Med. Phys.* **29** (12), 2788–2798.

GONG, J.X., CAO, L.H., PAN, K.Q., XIAO, K.D., WU, D., ZHENG, C.Y., LIU, Z.J. & HE, X.T. 2017 Enhancement of proton acceleration by a right-handed circularly polarized laser interaction with a cone target exposed to a longitudinal magnetic field. *Phys. Plasmas* **24** (5), 053109.

HONRUBIA, J., MORACE, A. & MURAKAMI, M. 2017 On intense proton beam generation and transport in hollow cones. *Matter Radiat. Extrem.* **2** (1), 28–36.

KURI, D.K., DAS, N. & PATEL, K. 2017 Proton acceleration from magnetized overdense plasmas. *Phys. Plasmas* **24** (1), 013112.

LI, X., CHAO, Y., XIE, R., LIU, D., ZHOU, Y., ZHANG, S., YANG, T., LIU, Z., CAO, L. & ZHENG, C. 2022 Enhancement of magnetic vortex acceleration by laser interaction with near-critical density plasma inside a hollow conical target. *Laser Part. Beams* **2022**, 5671790.

LV, C., ZHAO, B.-Z., WAN, F., CAI, H.-B., MENG, X.-H., XIE, B.-S., LIU, F.-L., LIU, Q.-S., ZHANG, X.-H., ZHANG, J., *et al.* 2019 Effect of the electron heating transition on the proton acceleration in a strongly magnetized plasma. *Phys. Plasmas* **26** (10), 103101.

MAKSIMCHUK, A., GU, S., FLIPPO, K., UMSTADTER, D. & BYCHENKOV, V.Y. 2000 Forward ion acceleration in thin films driven by a high-intensity laser. *Phys. Rev. Lett.* **84**, 4108–4111.

MIRANI, F., MAFFINI, A., CASAMICHIELA, F., PAZZAGLIA, A., FORMENTI, A., DELLASEGA, D., RUSSO, V., VAVASSORI, D., BORTOT, D., HUAULT, M., *et al.* 2021 Integrated quantitative PIXE analysis and EDX spectroscopy using a laser-driven particle source. *Sci. Adv.* **7** (3), eabc8660.

MORA, P. 2003 Plasma expansion into a vacuum. *Phys. Rev. Lett.* **90**, 185002.

NAKAMURA, T., BULANOV, S.V., ESIRKEPOV, T.Z. & KANDO, M. 2010 High-energy ions from near-critical density plasmas via magnetic vortex acceleration. *Phys. Rev. Lett.* **105**, 135002.

PASSONI, M., FEDELI, L. & MIRANI, F. 2019 Superintense laser-driven ion beam analysis. *Sci. Rep.* **9** (1), 9202.

ROBINSON, A.P.L., ZEPF, M., KAR, S., EVANS, R.G. & BELLEI, C. 2008 Radiation pressure acceleration of thin foils with circularly polarized laser pulses. *New J. Phys.* **10** (1), 013021.

SNAVELY, R.A., KEY, M.H., HATCHETT, S.P., COWAN, T.E., ROTH, M., PHILLIPS, T.W., STOYER, M.A., HENRY, E.A., SANGSTER, T.C., SINGH, M.S., *et al.* 2000 Intense high-energy proton beams from petawatt-laser irradiation of solids. *Phys. Rev. Lett.* **85**, 2945–2948.

TABAK, M., HAMMER, J., GLINSKY, M.E., KRUER, W.L., WILKS, S.C., WOODWORTH, J., CAMPBELL, E.M., PERRY, M.D. & MASON, R.J. 1994 Ignition and high gain with ultrapowerful lasers. *Phys. Plasmas* **1** (5), 1626–1634.

TOCHITSKY, S., PAK, A., FIUZA, F., HABERBERGER, D., LEMOS, N., LINK, A., FROULA, D.H. & JOSHI, C. 2020 Laser-driven collisionless shock acceleration of ions from near-critical plasmas. *Phys. Plasmas* **27** (8), 083102.

WAGNER, F., DEPPERT, O., BRABETZ, C., FIALA, P., KLEINSCHMIDT, A., POTH, P., SCHANZ, V.A., TEBARTZ, A., ZIELBAUER, B., ROTH, M., *et al.* 2016 Maximum proton energy above 85 MeV from the relativistic interaction of laser pulses with micrometer thick CH_2 targets. *Phys. Rev. Lett.* **116**, 205002.

WANG, H., CAO, L., ZHAO, Z., YU, M., GU, Y. & HE, X. 2012 Fast electron beam with manageable spotsize from laser interaction with the tailored cone-nanolayer target. *Laser Part. Beams* **30** (4), 553–558.

WILKS, S.C., LANGDON, A.B., COWAN, T.E., ROTH, M., SINGH, M., HATCHETT, S., KEY, M.H., PENNINGTON, D., MACKINNON, A. & SNAVELY, R.A. 2001 Energetic proton generation in ultra-intense laser–solid interactions. *Phys. Plasmas* **8** (2), 542–549.

XIE, R., CAO, L.H., CHAO, Y., JIANG, Y., LIU, Z.J., ZHENG, C.Y. & HE, X.T. 2020 Improvement of laser absorption and control of particle acceleration by subwavelength nanowire target. *Phys. Plasmas* **27** (12), 123108.

XIE, R., CAO, L.H., GONG, J.X., CHENG, H., LIU, Z.J., ZHENG, C.Y. & HE, X.T. 2019 Improvement of proton acceleration via collisionless shock acceleration by laser-foil interaction with an external magnetic field. *Phys. Plasmas* **26** (12), 123102.

YAN, X.Q., LIN, C., SHENG, Z.M., GUO, Z.Y., LIU, B.C., LU, Y.R., FANG, J.X. & CHEN, J.E. 2008 Generating high-current monoenergetic proton beams by a circularly polarized laser pulse in the phase-stableacceleration regime. *Phys. Rev. Lett.* **100**, 135003.

YANG, Y.C., ZHOU, C.T., HUANG, T.W., JU, L.B., JIANG, K., CAI, T.X., ZHANG, H., WU, S.Z., QIAO, B., YU, M.Y., *et al.* 2018 Proton acceleration from laser interaction with a complex double-layer plasma target. *Phys. Plasmas* **25** (12), 123107.

YU, J., ZHOU, W., CAO, L., ZHAO, Z., CAO, L., SHAN, L., LIU, D., JIN, X., LI, B. & GU, Y. 2012 Enhancement in coupling efficiency from laser to forward hot electrons by conical nanolayered targets. *Appl. Phys. Lett.* **100** (20), 204101.

ZHAO, Z., CAO, L., CAO, L., WANG, J., HUANG, W., JIANG, W., HE, Y., WU, Y., ZHU, B., DONG, K., *et al.* 2010 Acceleration and guiding of fast electrons by a nanobrush target. *Phys. Plasmas* **17** (12), 123108.